JOM, Vol. 66, No. 9, 2014
DOI: 10.1007/s11837-014-1032-x

Alloy Design, Combinatorial Synthesis, and Microstructure–Property Relations for Low-Density Fe-Mn-Al-C Austenitic Steels

D. RAABE,[1,3] H. SPRINGER,[1] I. GUTIERREZ-URRUTIA,[1,4] F. ROTERS,[1] M. BAUSCH,[1] J. -B. SEOL,[1] M. KOYAMA,[2] P. -P. CHOI,[1] and K. TSUZAKI[2]

1.—Max-Planck-Institut für Eisenforschung, 40237 Düsseldorf, Germany. 2.—Department of Mechanical Engineering, Kyushu University, 744 Motooka, Nishi-ku, Fukuoka, Fukuoka 819-0395, Japan. 3.—e-mail: d.raabe@mpie.de. 4.—e-mail: i.gutierrez@mpie.de

We present recent developments in the field of austenitic steels with up to 18% reduced mass density. The alloys are based on the Fe-Mn-Al-C system. Here, two steel types are addressed. The first one is a class of low-density twinning-induced plasticity or single phase austenitic TWIP (SIMPLEX) steels with 25–30 wt.% Mn and <4–5 wt.% Al or even <8 wt.% Al when naturally aged. The second one is a class of κ-carbide strengthened austenitic steels with even higher Al content. Here, κ-carbides form either at 500–600°C or even during quenching for >10 wt.% Al. Three topics are addressed in more detail, namely, the combinatorial bulk high-throughput design of a wide range of corresponding alloy variants, the development of microstructure–property relations for such steels, and their susceptibility to hydrogen embrittlement.

INTRODUCTION TO LOW DENSITY STEELS

Reducing energy consumption in conjunction with improving safety standards is a paramount target in modern mobility concepts. Hence, the development of strong, tough, and ductile steels for automotive applications is an essential topic in steel research.[1–15] In this context, twinning-induced plasticity (TWIP) steels with up to 30 wt.% Mn and >0.4 wt.% C content have shown an excellent combination of ductility and strength.[16–34] Increasingly, the reduction in mass density of TWIP steels becomes an additional challenge. Two effects enable such efforts. The first one is that Mn increases the face-centered cubic (fcc) lattice parameter. The second one is that very high Mn and C alloying stabilizes the austenite, so that it can tolerate Al additions up to about 10 wt.% without becoming unstable, i.e., transforming into body-centered cubic (bcc)-ferrite.[35]

Such an alloy concept sustains many advantages associated with TWIP steels, e.g., mechanical twinning and very high strain hardening;[16,19,24] yet, it enables density reductions of up to 18% (Fig. 1). Hence, alloys based on the quaternary system Fe-Mn-Al-C are specifically promising for the design of low-density TWIP steels.[36–47]

Regarding the excellent mechanical properties of TWIP steels, which are characterized by the transition from dislocation and cell hardening to massive mechanical twinning, it has to be considered that Al increases the stacking fault energy (SFE).[17,18] This means that the overall strain-hardening behavior and the onset of mechanical twinning in density-reduced TWIP grades[41] may differ from those observed in conventional TWIP steels.[17,19,24]

However, alloys based on the Fe-Mn-Al-C system offer an even larger variety in deformation and strain-hardening mechanisms than those associated with the TWIP effect alone. This is due to the characteristic dislocation substructures and the higher number of phases present in the Fe-Mn-Al-C system, namely, fcc-austenite, bcc-ferrite, and ordered structures such as DO_3 and $L'1_2$-type carbides. Depending on composition, low-density steels can assume austenitic structure for the composition regime Mn: 15–30 wt.%, Al: 2–12 wt.%, and C: 0.5–1.2 wt.%. To combine the advantages of the TWIP mechanisms with the reduction in specific weight,

(Published online June 24, 2014)

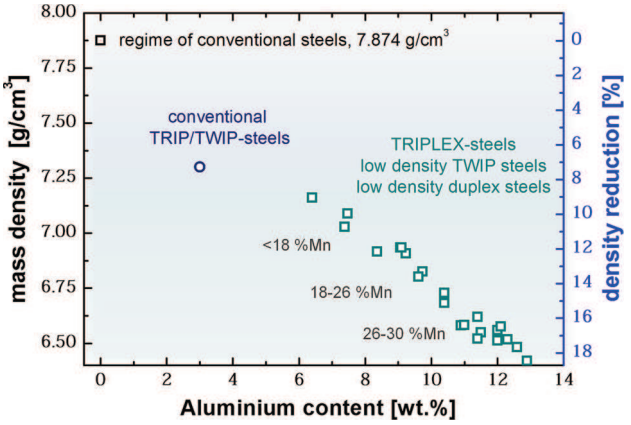

Fig. 1. Density reduction in Fe-Mn-Al-C TWIP steels as a function of Al content.

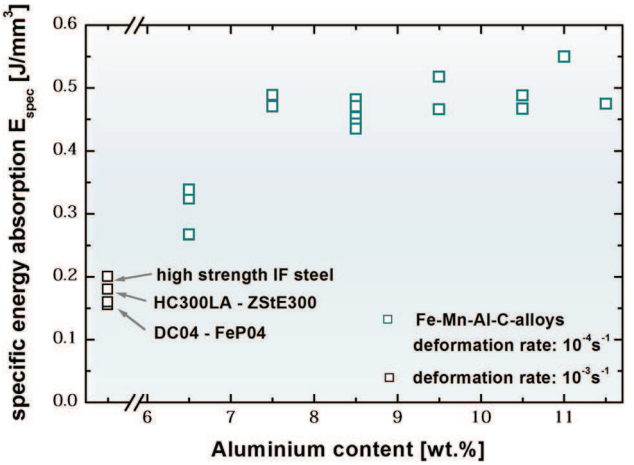

Fig. 2. Specific energy absorption values of selected Fe-Mn-Al-C steels in comparison with different conventional deep-drawing steels (Color figure online).

this alloy range is hence the most promising one. When increasing the Al content to a range >6–8 wt.%, strain hardening in these steels is less dominated by the TWIP effect but instead by the formation of nanosized L'1_2-type carbides, so-called κ-carbides.[44,45,48]

Density-reduced steels with ferritic structure have compositions in the range Mn < 8 wt.%, Al: 5–8 wt.%, and C < 0.3 wt.%. Corresponding complex grades, consisting of austenite and ferrite, can be synthesized by using compositions Mn: 5–30 wt.%, Al: 3–10 wt.%, and C: 0.1–0.7 wt.%.[48] Besides these compositions, ordered $D0_3$ structures, i.e., near-ferritic Fe-Al-Cr alloys without Mn, have also been addressed in the past in the context of density-reduced alloy design.

When comparing the synthesis and properties among the different classes of weight reduced steels, alloys based on the austenitic Fe-Mn-Al-C system are most attractive due to their superior strain hardening, high energy absorption (Fig. 2), high-density reduction and robust response to minor changes in composition and processing.[37–47] Even thin-strip casting with associated in-line hot rolling has been successfully conducted in our group as a pathway for efficient small-scale manufacturing of such grades.

Recent publications on austenitic Fe-Mn-Al-C alloys have reported yield strength values of 0.5–1.0 GPa, elongations to fracture in the range 30–80%, and ultimate tensile strength in the range of 1.0–1.5 GPa.[37–47]

When blended with an Al content below 5 wt.%, a single austenite phase prevails at room temperature, showing excellent strain hardening, which was attributed to the hierarchical evolution of the deformation substructure.[41] Al also promotes the formation of nanoprecipitates upon aging with L'1_2 structure and approximate stoichiometry of $(Fe,Mn)_3AlC$.[44,45,48] These phases are referred to as κ-carbides. They belong to the group of non-oxide perovskites. Because of their ordered fcc structure, κ-carbides have a lattice mismatch below 3% with respect to an austenitic Fe-Mn-C matrix phase and can hence form cuboidal nanoprecipitates.[44,48] When embedded in a ferritic matrix, the lattice mismatch can be as large as ~6%,[45,48] which leads to semicoherent interfaces and, hence, different precipitate morphologies.

This article provides a concise introduction to some recent developments in the field of low-density Fe-Mn-Al-C TWIP steels placing attention on alloy design, synthesis routes, and microstructure–property relations. We also provide a brief outlook on pending questions associated with the role of κ-carbides on strain hardening and hydrogen embrittlement.

BULK COMBINATORIAL DESIGN OF LOW-DENSITY AUSTENITIC STEELS

Here, we use a combinatorial approach for rapid trend screening and alloy maturation of metallurgically melted and processed Fe-Mn-Al-C low-density TWIP and κ-carbide hardened steels. The approach is referred to as rapid alloy prototyping (RAP).[49] We apply it here to one group of Fe-30Mn-1.2C-xAl (wt.%) TWIP steels and to a second group of Fe-20Mn-0.4C-xAl TWIP steels, both with varying Al content (x) and different aging conditions.

In both cases, the samples were synthesized by melting and casting in a vacuum-induction melting (VIM) furnace under 400 mbar Ar pressure. The system was modified to enable synthesis of five different alloys in one operation for each alloy system. We used five Cu molds, which could be moved stepwise inside the furnace. They were successively filled with melt from a 4-kg ingot. After each cast, the remaining melt composition in the ingot was adjusted by charging Al through an air lock. After cooling and cutting, the 10 × 50 × 130-mm^3-sized blocks were hot rolled at 1100°C into 2 ± 0.1-mm-

thick and ~500-mm-long sheets. These were reheated to 1100°C, water quenched, and cut perpendicular to the rolling direction into sets of nine segments with dimensions $2 \times 60 \times 55$ mm^3 for each alloy composition. Homogenization was performed at 1100°C for 2 h under Ar, followed by water quenching. Aging was conducted in air at 450°C, 500°C, 550°C, and 600°C for 0 h, 1 h, and 24 h at each temperature, followed by oil quenching. This results in a matrix of 45 different sample conditions. Scales were removed from the surfaces by low-pressure, fine-grit sandblasting after the heat treatments. Samples for mechanical testing and microstructure investigation were prepared from the segments by package spark erosion. Tensile testing was conducted at room temperature with an initial strain rate of 10^{-3} s^{-1}. All values plotted represent averages of three measurements for every material state. Cross-sectional areas of selected samples were prepared in the plane perpendicular to the rolling direction by grinding and polishing with standard metallographic techniques. X-ray diffraction (XRD) analysis was performed on the rolling plane of samples ground to a thickness of 1 mm. Further details of the method are explained in Ref. 49.

The RAP method enabled us to screen two different sets of five Fe-Mn-C-based weight-reduced Al-containing compositions each exposed to nine respective heat treatments within 35 h. For each alloy base set, synthesis, processing, mechanical screening, and phase characterization are included. The metallographic analysis showed no cracks, pores, or macrosegregations in the final materials. The as-cast samples had a coarse dendritic microstructure. Hot rolling and water quenching resulted in a fully recrystallized microstructure with a grain size of ~20 μm with some retained microsegregations of Mn.

Figure 3 shows the mechanical properties of 45 different material conditions obtained for the Fe-30Mn-1.2C base composition (i.e., in total 135 tensile tests and hardness measurements) in terms of the yield strength (YS, Fig. 3a), ultimate tensile strength (UTS, Fig. 3b), total elongation (TE, Fig. 3c), and hardness (Fig. 3d). The results are plotted according to the systematically varied Al content. Color-coding reflects individual aging conditions. The data are reproduced from an earlier publication.[49] They show a clear dependence of the mechanical behavior on both composition and heat treatment.

For the reference material (no Al addition, i.e., ternary Fe-30Mn-1.2C alloy), the best mechanical behavior is found for the as-homogenized state, namely, 360 MPa YS, high work hardening (830 MPa UTS), and high ductility (77% TE). Aging of the Fe-30Mn-1.2C alloy leaves the YS virtually unchanged and increases the hardness slightly. However, it reduces UTS and TE. Embrittlement becomes most apparent for long aging times (24 h) and higher temperatures (>500°C). For the alloy Fe-30Mn-1.2C-8Al, i.e., the material with the highest Al content and lowest density, the opposite trend applies. Without aging, the mechanical response is similar to that of the Al-free alloy. Only a minor change in YS (increase), UTS, and TE (decrease) is found. Aging for 1 h leads to an increase in YS, UTS, and hardness (increasing with temperature) and only to a minor reduction in TE. Aging of the alloy Fe-30Mn-1.2C-8Al for 24 h further increases YS, UTS, and hardness to levels twice as high as in the as-homogenized state and drastically reduces ductility. The mechanical data for the alloys with intermediate Al contents fall between the two different behaviors described above, i.e., alloys with 2–6 wt.% Al have properties between the respective values from materials without Al and with 8 wt.% Al. Especially the alloys with Al additions of 4 wt.% and 6 wt.% are only very weakly affected by the applied aging treatments in terms of their mechanical data compared with the alloys Fe-30Mn-1.2C (weakening/embrittlement) and Fe-30Mn-1.2C-8Al (strengthening). To better extract the mechanical trends for the investigated compositions and heat treatments, selected results are summarized in Fig. 4.

By using the RAP approach, we find for the 30 wt.% Mn system that high amounts of Al (~8 wt.%) result in pronounced strengthening during aging, depending on time and temperature (Fig. 4). The observed effects are attributed to the formation of nm-sized κ-carbides during aging. The intermediate alloy variants with Al concentrations of 2–6 wt.% do not show equivalent mechanical properties compared to the ~8 wt.% Al variant. Also, a much smaller influence of aging on the tensile behavior can be observed in the 2–6 wt.% Al cases. A detailed and systematic screening of the stoichiometry, interface structure, lattice misfit, and mechanical effects of the nm-sized κ-carbides is still pending, but first results suggest that they can occur in a wide compositional existence range (Fig. 5). Also it is observed that they are thermally very stable at 600°C and even prevail after 100 h heat treatment with only modest coarsening (Fig. 5).

For the second alloy class investigated, namely, the Fe-20Mn-0.4C-xAl TWIP steels, a more homogeneous trend of the mechanical properties as a function of the Al content is observed (Fig. 6). While yield strength and ultimate tensile strength both increase, the tensile elongation drops as a function of the Al content in the range between 2 wt.% and 11 wt.% Al. As observed by XRD screening of the corresponding samples, the increasing ferrite content seems to be more relevant for this trend than the presence of κ carbides or ε-martensite.

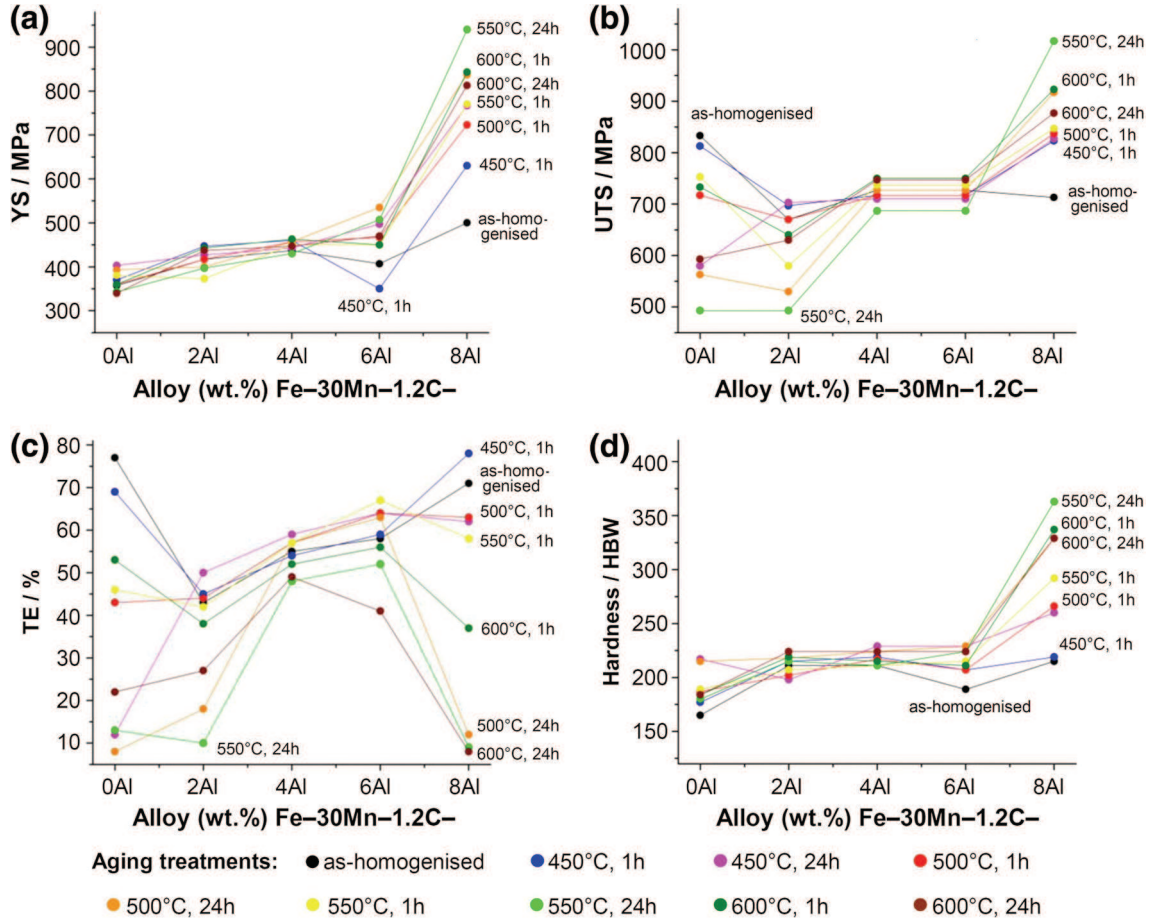

Fig. 3. Overview of the obtained mechanical properties from RAP experiments as a function of alloy composition and applied aging treatment: (a) yield stress (YS), (b) ultimate tensile stress (UTS), (c) total elongation (TE), (d) hardness. (RAP: Rapid Alloy Prototyping). Data and figures are reproduced from an earlier publication[49] (Color figure online).

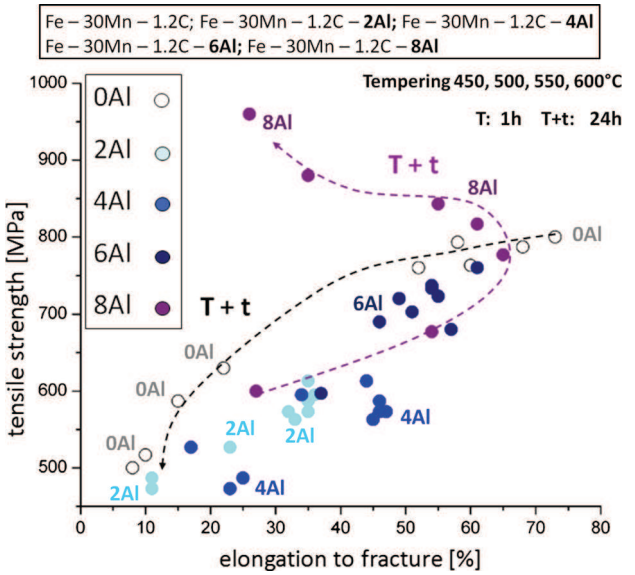

Fig. 4. Selected mechanical testing results from RAP experiments: Tensile strength and total elongation for alloys Fe-30Mn-1.2C through Fe-30Mn-1.2C-8Al. Some data were taken from Ref. 49 (Color figure online).

MICROSTRUCTURE–PROPERTY RELATIONS FOR LOW-DENSITY AUSTENITIC STEELS

When deriving microstructure–property relationships for austenitic low-density steels, two scenarios must be considered: For compositions with 25–30 wt.% Mn and up to 4–5 wt.% Al or even 8 wt.% Al, when naturally aged, the TWIP effect prevails as deformation mechanism.[41,48] Thus, dislocation-based strain hardening, which is followed at higher loads by mechanical twinning, is the primary strain-hardening mechanism. Such low-density TWIP alloys are referred to as single phase austenitic TWIP (SIMPLEX) steels.[48] After aging at 500–600°C or for alloys with higher Al content, twinning is reduced and strain hardening is essentially associated to κ-carbide and solid-solution strengthening (Figs. 5 and 6).

If the Al content exceeds 10 wt.%, then κ-carbides can form during quenching. The exact strain-hardening mechanism for the latter case is still under investigation. In a recent study, Gutierrez-Urrutia and Raabe[48] suggested that the prevalent deformation

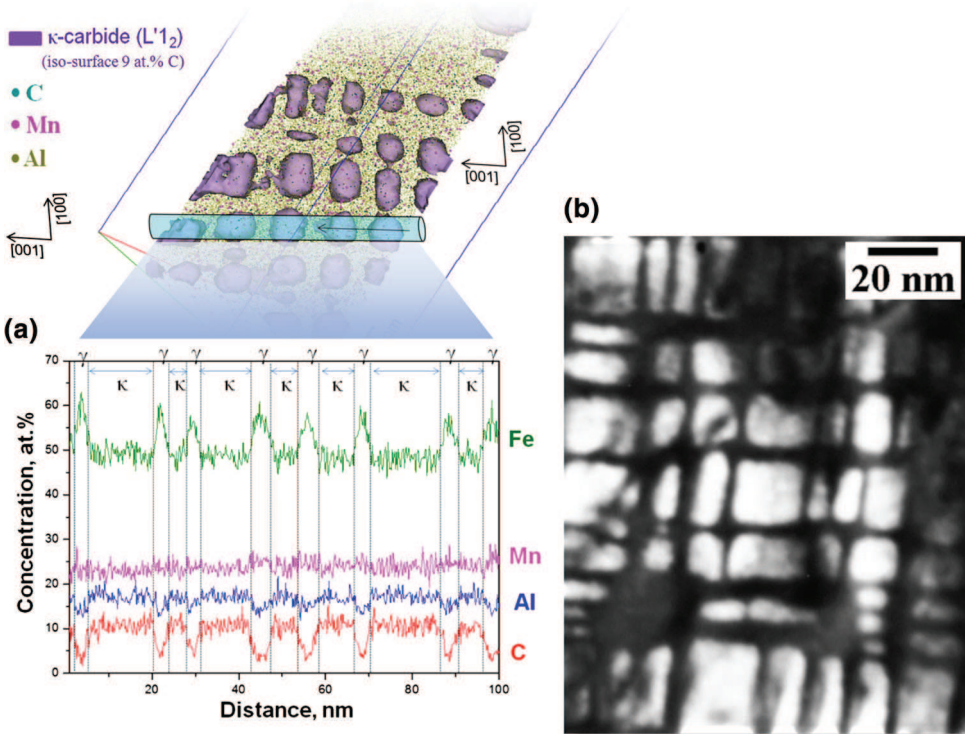

Fig. 5. (a) Joint atom probe tomographic and (b) Transmission Electron Microscopy (TEM) analysis of κ-carbides in a Fe-30Mn-1.2C-8Al low-density steel after 24 h at 600°C. This sample was synthesized after identifying suited compositions by the RAP process (Color figure online).

mechanisms in austenitic steels that are strengthened by regularly arranged nanosized κ-carbides, such as those shown in Fig. 5, consist in Orowan bypassing of longitudinal rods of κ-carbides and subsequent expansion of dislocation loops, which is assisted by dislocation cross-slip and, to a minor extent, shearing of κ-carbides.

They further suggest that the higher dislocation densities observed within the dislocation bundles are caused by minor topological differences in the spacing between the κ-carbide rods, so that dislocations follow preferential soft paths within the widest channels. In certain cases, these dislocation accumulations can lead to stress values that are high enough to shear κ-carbide interfaces. Although these complex nanoscale interactions are still subject to further analysis, we give below some suggestions how to incorporate such effects into a mean field dislocation density-based model of strain hardening of κ-carbide containing Fe-Mn-Al-C steels.

A general form of a temperature-sensitive constitutive model for fcc metals with low stacking fault energy and mechanical twinning, depending on chemical composition, deformation rate, and temperature, was introduced by Steinmetz et al.[50] It extends the three-internal-variable model of Roters et al.[51] with a physical description of twin nucleation. The model is based upon experimental observations performed on Fe-Mn-C TWIP steels (without κ-carbides) by electron channeling contrast imaging, Transmission Electron Microscopy (TEM), and electron backscatter diffraction (EBSD).[19–34] These works revealed that the important microstructural internal state variables in such alloys include dislocations, grain size, mechanical twins, and dislocation cells. In this regard, this model provides a quantitative description of strain-hardening behavior of low-density TWIP steels, i.e., SIMPLEX steels. Following the comments made above, strain hardening in κ-carbide-containing steels can be described in a seamless fashion where the activation barrier for twinning can vary as a function of the Al content and a carbide-rod-dependent Orowan loop mechanism can be introduced in the form of a corresponding stress term in the kinetic equation of state. The latter formulation is not yet presented here.

In this section, we provide a summarized description of the temperature-sensitive constitutive model of strain hardening for single-phase low-density TWIP steels, i.e., SIMPLEX steels. The model uses three different dislocation densities (ρ_c, ρ_w, and ρ_d) and the volume fraction of mechanical twins (f_{tw}) as state variables. The three dislocation densities are those in the cell interior, in the cell walls, and dipoles. The evolutions of these state variables represent the microstructural changes that occur during plastic deformation. The evolution of the dislocation densities is given by the following equations:

$$\dot{\rho}_c = \frac{\dot{\varepsilon} M}{b}\left(\frac{1}{\Lambda_c} - \frac{2d_d}{n}\rho_c\right) \tag{1}$$

$$\dot{\rho}_{\mathrm{w}} = \frac{\dot{\varepsilon} M}{b}\left(\frac{1}{\Lambda_{\mathrm{w}}} - \frac{2 d_{\mathrm{d}}}{n}\rho_{\mathrm{w}}\right) \tag{2}$$

$$\dot{\rho}_{\mathrm{d}} = 2\frac{\dot{\varepsilon} M}{bn}\left\{(d_{\mathrm{d}} - d_{\mathrm{a}})\left[\rho_{\mathrm{w}} + \rho_{\mathrm{c}}\left(\frac{f_{\mathrm{c}}}{f_{\mathrm{w}}}\right)\right] - d_{\mathrm{a}}\rho_{\mathrm{d}}\right\} - \frac{2\rho_{\mathrm{d}} v_{\mathrm{climb}}}{d_{\mathrm{d}} - d_{\mathrm{a}}} \tag{3}$$

where $\dot{\varepsilon}$ is the externally imposed strain rate; b = 2.56 Å the Burgers vector; $M = 3.06$ the Taylor factor; $n = 3$ a constant for the average number of active slip systems; $f_{\mathrm{c}} + f_{\mathrm{w}} = 1$ are the volume fractions of the dislocation cell interiors and the dislocation cell walls, set to 0.9 and 0.1, respectively; and d_{a} is the minimum stable dipole distance before spontaneous annihilation occurs. The dislocation climb velocity is given by:

$$v_{\mathrm{climb}} = \frac{D_0}{kT}\frac{G\Omega}{\pi(1-\nu)d_{\mathrm{d}}}\exp\left(\frac{-Q_{\mathrm{c}}}{kT}\right) \tag{4}$$

$D_0 = 4.0 \times 10^{-5}\,\mathrm{m^2\,s^{-1}}$ is the self-diffusion coefficient, ν is the Poisson ratio, G is the shear modulus, Ω is the activation volume for climb, and Q_{c} is the vacancy formation and migration energy. d_{d} the maximum glide plane spacing two dislocations can have to form a dipole, is calculated as:

$$d_{\mathrm{d}} = \frac{Gb}{8\pi(1-\nu)\tau_{\mathrm{eff,W}}} \tag{5}$$

The derivation of the evolution equations and evolution of the dislocation densities is described in Ref. 51. The glide resistance is calculated from the following equation:

$$\hat{\tau} = \tau_0 + \alpha G b\sqrt{\rho} \tag{6}$$

Separate glide resistances are calculated for the cell interior and the cell wall due to the individual dislocation densities. The variable α is a geometry factor, b is the magnitude of the Burgers vector, ρ is the dislocation density, and τ_0 is the strength due to solid solution. The latter parameter is used to capture the effects of the solute Mn, Al, and C. The strain rate is expressed as:

$$\dot{\varepsilon} = \frac{\dot{\gamma}}{M} = \frac{\lambda v_0 b \rho}{M}\exp\left(-\frac{\Delta G}{kT}\right) \tag{7}$$

where $\dot{\gamma}$ is the shear rate, λ is the dislocation spacing calculated by $\lambda = 1/\sqrt{\rho_x}$ where x represents c or w, v_0 is the Debye frequency, ρ is the mobile dislocation density, and ΔG is the activation energy for slip. A modified glide resistance profile as introduced by Kocks et al.[52,53] is used. The activation energy is therefore taken as:

$$\Delta G = Q_{\mathrm{s}}\left[1 - \left(\frac{\tau_{\mathrm{eff}}}{\hat{\tau}}\right)^p\right]^q \tag{8}$$

The variables p and q are fitting parameters that control the obstacle profile, τ_{eff} is the resolved shear stress, and Q_{s} is the total free energy required to overcome an obstacle without the aid of external work. This type of obstacle model can also serve to capture the effect of the κ-carbides. Inserting Eq. 8 into Eq. 6 leads to:

$$\dot{\varepsilon} = \frac{\lambda_x v_0 b \rho_x}{M}\exp\left\{-\frac{Q_{\mathrm{s}}}{kT}\left[1 - \left(\frac{\tau_{\mathrm{eff},x}}{\tau_0 + \alpha G b\sqrt{\rho_x}}\right)^p\right]^q\right\} \tag{9}$$

where x represents c or w. As mentioned above, the resolved shear stress is calculated individually for the cell interior ($\tau_{\mathrm{eff,c}}$) and the cell walls ($\tau_{\mathrm{eff,w}}$), where for the cell walls, $\rho_x = \rho_w + \rho_d$. The two shear stresses are combined via a mixing law to form an averaged resolved shear stress (τ_{rss}), used later in Eqs. 24 and 26 to calculate the probability of twin nucleation:

$$\sigma_{\mathrm{ext}} = M\tau_{\mathrm{rss}} = M\left(f_{\mathrm{c}}\tau_{\mathrm{eff,c}} + f_{\mathrm{w}}\tau_{\mathrm{eff,w}}\right) \tag{10}$$

When dislocation densities serve as primary state variables for describing hardening, the ratio between the increment in slipped area and the increment in (deposited) dislocation length is the decisive measure resulting in strain hardening:

$$d\rho = \frac{d\gamma}{b\Lambda} \tag{11}$$

The parameter Λ is referred to as the mean free path (MFP). In reality, numerous phenomena contribute to it and its change upon straining such as grain size, existing forest dislocations, and—in the current case—the twin spacing or κ-carbides, respectively. The symbols i_{c} and i_{w} are fitting parameters that are the average number of dislocation spacings that a dislocation moves before rendered sessile. It is the analogue to the reciprocal of the fitting parameter k used in similar models;[52,53] however, here it has a crisp physical meaning. We use a harmonic mean to calculate the MFP, one in the cell interior and one in the cell wall:

$$\frac{1}{\Lambda_{\mathrm{c}}} = \frac{\sqrt{\rho_{\mathrm{c}}}}{i_{\mathrm{c}}} + \frac{1}{d} + \frac{1}{i_{\mathrm{tw}} t} \tag{12}$$

$$\frac{1}{\Lambda_w} = \frac{\sqrt{\rho_w + \rho_d}}{i_w} + \frac{1}{d} + \frac{1}{i_{\mathrm{tw}} t} \tag{13}$$

The symbol Λ_{c} represents the MFP of single mobile dislocations inside dislocation cells, Λ_w the MFP of single mobile dislocations inside dislocation cell walls, d the grain size, and t the MFP due to twins. When strain hardening is not determined by twins but instead by rods consisting of κ-carbides, the mean spacing among wide rod channels could enter

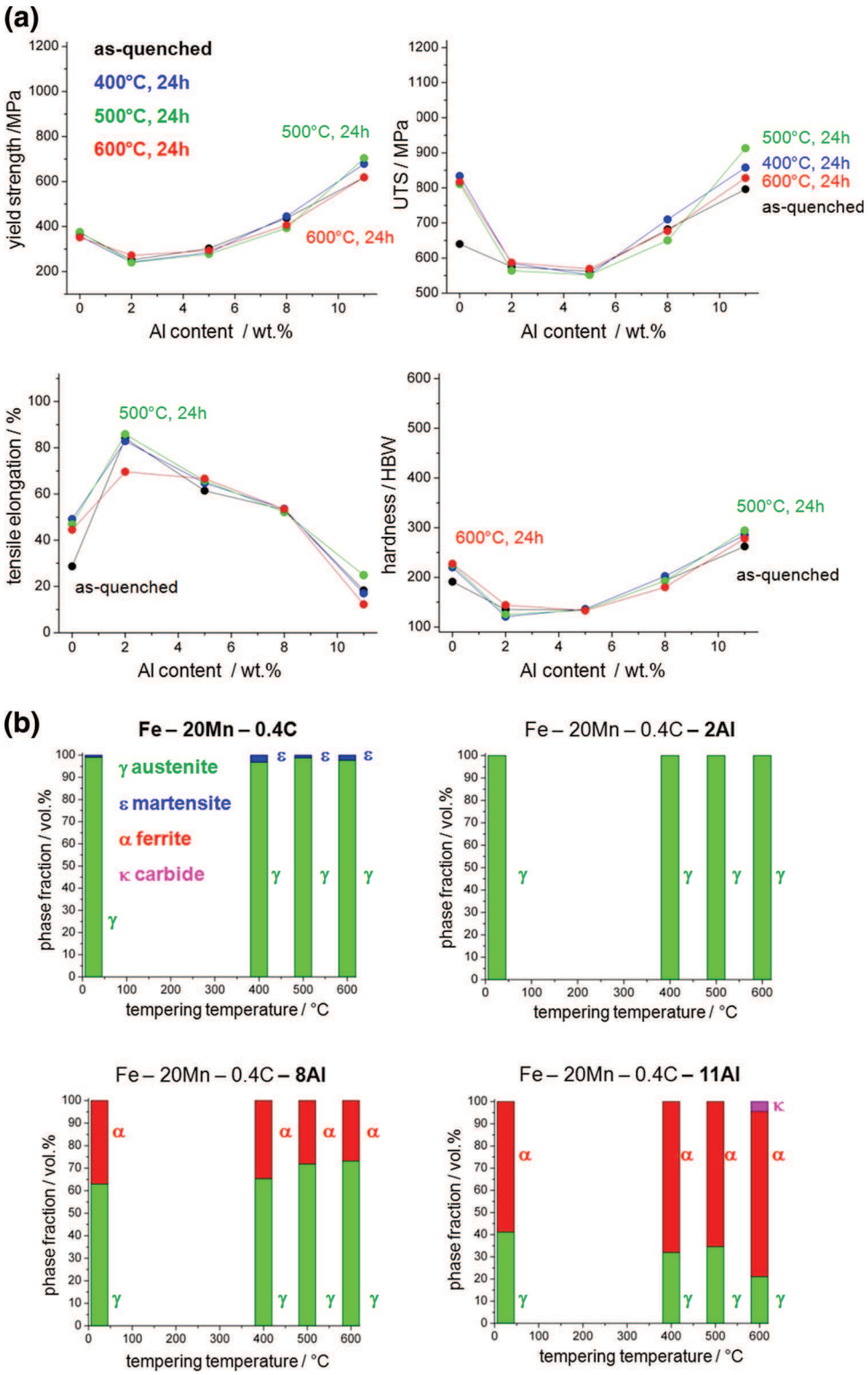

Fig. 6. Selected bulk combinatorial screening results for another low-density TWIP steel system, namely, Fe-20Mn-0.4C-*x*Al (wt.%): (a) tensile and hardness testing data as a function of tempering (aging) temperature and Al-content and (b) corresponding XRD analysis, linking the observed strengthening and embrittlement phenomena to the constituting phases (Color figure online).

as a further contribution to the harmonic mean. It is not clear though at this stage whether instead Orowan looping inside these channels would be a more adequate description. In case of a TWIP alloy, the number of twin spacings a dislocation travels before becoming sessile in the case of twinning is i_{tw}.

The twinning MFP evolves according to the stereological relationship developed by Fullman:[54]

$$\frac{1}{t} = \frac{1}{2e}\frac{f_{tw}}{(1-f_{tw})} \tag{14}$$

where f_{tw} is the twin volume fraction and e is the average twin width, or average with of a twin bundle if they exist. A discussion of the evolution of f_{tw} is given below. Here, we use the twin nucleation mechanism of Mahajan and Chin.[55] The twin nucleus is formed by three stacking faults on adjacent (111) planes. The critical event for the growth of the nucleus into a twin is the bow out of the three partial dislocations between the pinning points separated by L_0. Twin growth is determined by the overall energy of the system calculated from three contributions:

$$Q_{work} = -3b_s\tau A(r, L_0) \tag{15}$$

$$Q_{sf} = \gamma_{sf} A(r, L_0) \tag{16}$$

$$Q_{line} = \frac{9}{2} G b_s B(r, L_0) \tag{17}$$

where Q_{work} is the energy supplied by the applied shear stress τ, Q_{sf} is the energy required to extend the stacking fault, and Q_{line} is the energy required to extend the dislocation lines. The symbol γ_{sf} represents the stacking fault energy, b_s is the Burgers vector of the Shockley partial, $A(r, L_0)$ is an area function and $B(r, L_0)$ is the dislocation line length. The total energy of the system is then:

$$Q_{total} = Q_{work} + Q_{sf} + Q_{line} \tag{18}$$

For high applied stresses, the energy is constantly decreasing, but for a particular stress level, a saddle point is found at $2r = L_0$. The saddle point is very sharp in stress, creating a steep increase in the activation barrier for small decreases of the stress, resulting in an essentially athermal barrier stress. At this point, the mobile partial dislocations will have formed a semicircle between the two pinning points. The stress at this configuration is defined as the critical twinning stress for twin formation and is given by:[50]

$$\tau_{tw} = \frac{\gamma_{sf}}{3b_s} + \frac{3Gb_s}{L_0} \tag{19}$$

The stacking fault energy plays an important role in defining the critical twinning stress. As it is strongly temperature dependent, thermodynamically calculated stacking fault energies by the method of Saeed-Akbari et al.[56] and corrected by ab initio calculations[35] were used.

The total number of potential twin nuclei is calculated based on the dislocation reaction that creates the nucleus. The number of active slip systems is a user-set parameter in the model. If the number of active systems is set to three, then the probability that all three randomly chosen slip systems will be non-coplanar is 54/110. Hence, the probability for having two active slip systems that are coplanar, fulfilling a necessary criterion for the formation of the twin nucleus, is $1 - 54/110 = 56/110$. Dislocations can only form the twin nucleus in the given model when their interaction is repulsive, i.e., 50% of the time. The product of the statistical chance of forming a twin nucleus, the change in dislocation density due to dislocation multiplication accommodating the externally imposed strain rate, and the reciprocal of the length of partial dislocations in one twin nucleus, $2/(3L_0)$, gives the number density of potential twin nuclei per unit time:

$$p_{st} = \frac{56}{110}\frac{\dot{\varepsilon}M}{2}\frac{2}{3L_0}\rho = \frac{28}{165}\frac{\dot{\varepsilon}M}{L_0}[\rho_c f_c + (\rho_w + \rho_d)f_w] \tag{20}$$

In Mahajan and Chin's nucleation model, one bounding partial dislocation from each of two extended stacking faults on the same slip plane must come within a critical distance of one another, set as $x_c = 10\text{A}$ for the extreme case. The equilibrium separation of Shockley partials in fcc metals is calculated as:

$$x_0 = \frac{Gb_s}{\gamma_{sf}}\frac{b_s}{8\pi}\frac{2+\nu}{1-\nu}, b_s = \frac{b}{\sqrt{3}} \tag{21}$$

The repulsive force between the two partials is given by:[55]

$$F_r = \frac{Gb_s^2}{2(x_0 + x_c)} + \frac{Gb_s^2\cos(\pi/3)}{2\pi x_0} \tag{22}$$

Therefore, the stress needed to bring the two partials to within the critical distance to form the twin nucleus, x_c, without help from an external applied shear stress is

$$\tau_r = F_r/b_s \tag{23}$$

For this stress to develop, a dislocation pile-up must occur creating a stress concentration. As the dislocations pile up, the partials could be forced to recombine into the full dislocation. If the dislocation is of screw character, then it could cross-slip to another plane and relax some of the stress caused by the dislocation pile-up. The probability that a cross-slip event will not occur, which instead allows a sufficient number of dislocations to pile up and form the stress concentration necessary to form the twin nucleus, is given by

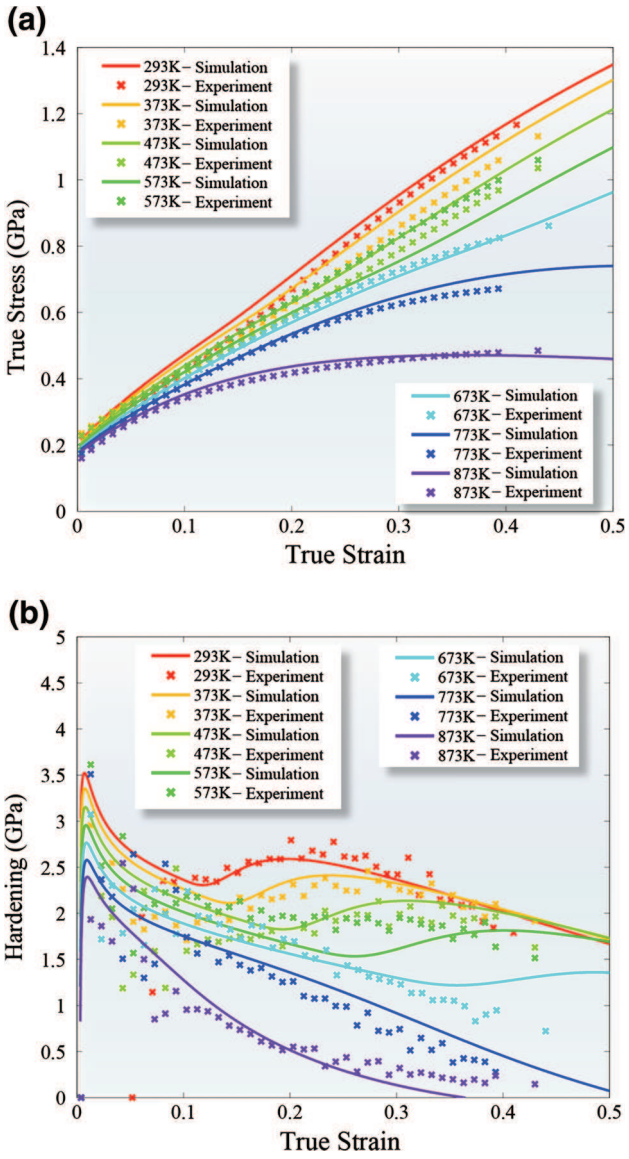

Fig. 7. (a) True stress–strain compression curves for a Fe-22wt.% Mn-0.6wt.% C model TWIP steel at seven different temperatures. One coherent parameter set was used for the whole temperature range. Data are taken from Ref. 50. (b) Strain-hardening curves corresponding to the true stress–true strain curves in Fig. 1a. Fe-22wt.% Mn-0.6wt.% C model TWIP steel at seven different temperatures. One coherent parameter set was used for the whole temperature range. Data taken from Ref. 50 (Color figure online).

$$p_{\mathrm{ncs}} = 1 - \exp\left[-\frac{V}{kT}(\tau_{\mathrm{r}} - \tau_{\mathrm{rss}})\right] \tag{24}$$

where V is the cross-slip activation volume. The total number density of twin nuclei per unit time is then

$$\dot{\theta} = p_{\mathrm{st}} p_{\mathrm{ncs}} \tag{25}$$

The probability that the triple-layer stacking fault bows out to form a twin (i.e., that a nucleation event occurs) is

$$p_{\mathrm{tw}} = \exp\left[-\left(\frac{\tau_{\mathrm{tw}}}{\tau_{\mathrm{rss}}}\right)^{s}\right] \tag{26}$$

where τ_{tw} is shown in Eq. 19 and s is a fitting parameter determining the sharpness of the transition from the non-twinning to twinning stress domain. It can be used to represent the effect that texture has on determining the percentage of grains which twin.

The total twin nucleation rate ($\dot{N}$) is calculated by multiplying the total number density of potential twin nuclei per unit time (p_{st}) by the probability that a sufficient stress concentration for the formation of the nucleus exists (p_{tw}) by the probability that one of those nuclei grows and develops into a twin (p_{ncs}):

$$\dot{N} = \dot{\theta} p_{\mathrm{tw}} = p_{\mathrm{st}} p_{\mathrm{ncs}} p_{\mathrm{tw}} \tag{27}$$

As during twin growth, energy is always gained; it is assumed that twins grow instantaneously until they encounter an obstacle such as a grain boundary or a twin on a noncoplanar twin system. A new twin is considered to be disk shaped, where the radial dimension is based on the average twin spacing. The twin volume is then given by

$$V_{\mathrm{tw}} = \frac{\pi}{4} e t^2 \tag{28}$$

where t is the average twin spacing from Eq. 14 and e is the average twin width. It is treated as a constant and is set to 30 nm based on experimental observations. Finally, the twin volume fraction evolution is calculated by the product of the nucleation rate, the volume that a new twin occupies, and the untwinned volume:

$$\dot{f}_{\mathrm{tw}} = (1 - f_{\mathrm{tw}}) \dot{N} V_{\mathrm{tw}} \tag{29}$$

Further details such as the incorporation of temperature are given in Ref. 50.

With this general form of an fcc strain-hardening model for alloys with low SFE, experimental results over a wide range of temperatures can be realistically simulated using a single parameter set. Here, we provide evidence of the robustness of the model by illustrating both experimental and simulated flow curves of a Fe-22wt.%Mn-0.6wt.%C TWIP model alloy at different deformation conditions (data taken from Ref. 50). Figure 7a shows the flow curves for a set of seven different temperatures, and Fig. 7b shows the strain-hardening curves corresponding to the stress–strain curves in Fig. 7a.

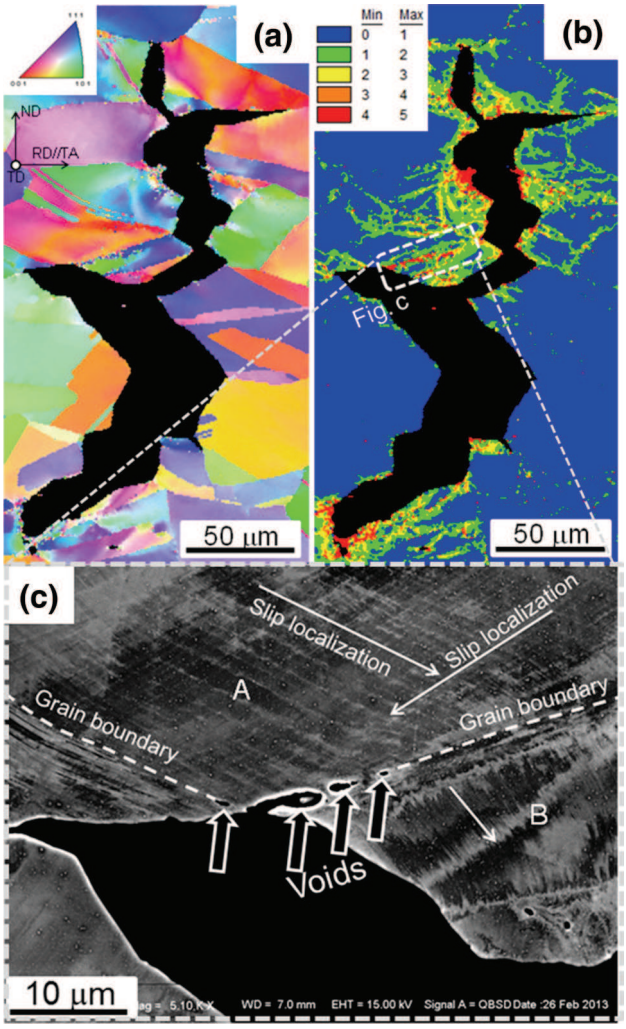

Fig. 8. (a) Inverse pole figure texture mapping obtained by EBSD (RD-IPF). (b) KAM map obtained from the EBSD-derived orientation gradients. The KAM values were calculated using the first neighboring EBSD point shell at a spacing of 300 nm. (c) Orientation-optimized ECCI corresponding to the part surrounded by the white lines in (b). (KAM: Kernel average misorientation; RD: longitudinal direction; IPF: inverse pole figure; ECCI: Electron Channeling Contrast Imaging). Data are taken from Ref. 59 (Color figure online).

THE EFFECT OF HYDROGEN ON THE MICROSTRUCTURE AND MECHANICAL BEHAVIOR OF LOW-DENSITY AUSTENITIC STEELS

Like for other steels approaching or exceeding 1 GPa in tensile strength, hydrogen embrittlement becomes an essential challenge also for TWIP grades.[57,58] Corresponding hydrogen-assisted fracture effects in a low-density austenitic steel were recently studied by our group[59] More specific, the influence of hydrogen on the tensile ductility of a κ-carbide hardened austenitic low-density steel with composition Fe-26Mn-11Al-1.2C (wt.%) was studied under direct, i.e., permanent, hydrogen charging.

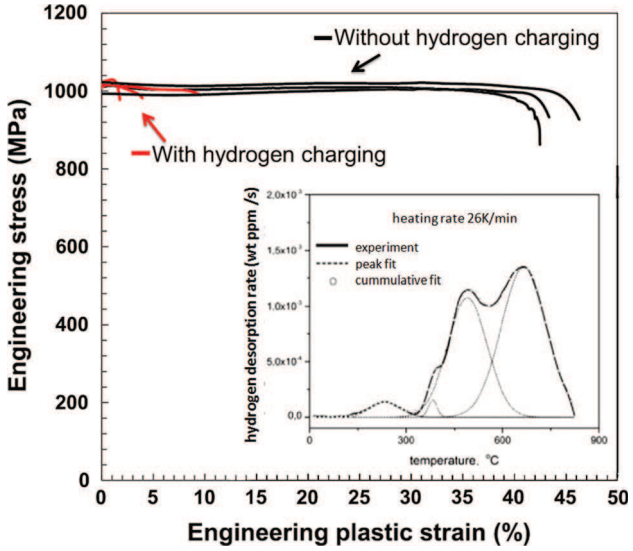

Fig. 9. Stress–strain tests conducted on specimens with and without hydrogen charging. In this approach, hydrogen was introduced into the samples via precharging for 40 min as well as permanent in situ hydrogen charging imposed also during the ongoing tests. The inset image shows results obtained from thermal desorption analysis taken at a heating rate of 26 K/min (Color figure online).

The hydrogen-induced micromechanisms pertaining to crack formation and crack propagation were studied by employing a joint probing approach using EBSD in conjunction with electron-channeling contrast imaging (ECCI)[30–34] The observed embrittlement effects in this alloy were mainly due to two distinct phenomena. The first damage-initiation mechanism was characterized by cracking at grain boundary triple junctions. The second mechanism was characterized by the gradual formation of chains of microvoids that formed on grain boundaries under the influence of pronounced planar slip localization (Fig. 8).[59] This effect entailed void coalescence and intergranular cracking along the grain boundaries affected. It was suggested that specifically the latter mechanism, i.e., intense slip localization, was linked to the presence of κ-carbides in this steel.

By using thermal desorption analysis, Koyama et al.[59] observed that the κ-carbides can act as hydrogen trap sites with an estimated activation energy of ~76–80 kJ/mol as obtained from a corresponding Redlich–Kister analysis (Fig. 9).

Thus, while κ-carbide precipitates could on the one hand act as beneficial trapping sites that might render hydrogen immobile, on the other hand the associated hydrogen-assisted planar slip acts in the opposite direction by promoting grain boundary void formation.

SUMMARY AND OUTLOOK

We presented an approach for the metallurgical bulk-scale high-throughput synthesis and processing of low-density austenitic steels. As model sys-

tem, we have chosen Fe-Mn-Al-C steels that exhibit a wide spectrum of characteristics. To reduce the density of such materials, the focus was placed on the effect of variations in the Al concentrations in the range between 0 wt.% and 11 wt.%. For weight measurements, some alloys with up to 13 wt.% Al were synthesized, revealing a reduction in density by about 18%. Additionally, two different Fe-Mn-C base compositions were screened, namely one with 20 wt.% Mn and 0.4 wt.% C and the other one with 30 wt.% Mn and 1.2 wt.% C. This relatively large set of material data showed that increasing the Al content promotes the formation of κ-carbides and ferrite. In case that a single-phase austenite matrix is desired, the ferrite stabilizing effect of Al must be compensated by an increased Mn and C content. The latter balance is also of very high relevance for optimizing the stacking fault energy that controls the TWIP effect. Two types of austenitic Fe-Mn-Al-C steels were addressed in more detail. The first one is a type of low-density TWIP (or SIMPLEX) steel with 25–30 wt.% Mn and $<$4–5 wt.% Al. The second one is a class of κ-carbide strengthened steel with the same chemical composition than the SIMPLEX steel and aged at 500–600°C or with higher Al content (above 10 wt.%). In the latter case, κ-carbides were observed to form during quenching.

The strain-hardening characteristics of low-density austenitic steels were discussed in terms of a structure–property constitutive model. The high strain-hardening capability of the low-density TWIP steel results from the onset of mechanical twinning at rather high stress levels. Therefore, it is important in corresponding alloy design strategies for low-density TWIP steels to consider a relatively high content in both Mn and C. Otherwise, the stacking fault energy becomes too high and twinning might become ineffective or suppressed.

The role of κ-carbides on the strain-hardening behavior of the non-TWIP variants was discussed in terms of Orowan bypassing of elongated rods of such carbides. Further strain-hardening effects associated with κ-carbides are still subject to further work owing to our still limited knowledge about the interaction of dislocations, twins, and κ-carbides. Likewise, the role and the alloying limits of a further increased C content and its effect on decoration, localization, nonlinear effects, and cross slip of dislocations is not yet clear and requires further research.

ACKNOWLEDGEMENTS

The authors are deeply indebted to the late Professor Georg Frommeyer for his guidance in designing low-density steels. Some of the data shown in Figs. 1 and 2 stem from his work.

REFERENCES

1. J.G. Speer, D.K. Matlock, B.C. De Cooman, and J.G. Schroth, *Acta Mater.* 51, 2611 (2003).
2. D. Barbier, N. Gey, S. Allain, N. Bozzolo, and M. Humbert, *Mater. Sci. Eng. A* 500, 196 (2009).
3. F.G. Caballero and H.K.D.H. Bhadeshia, *Curr. Opin. Solid State Mater. Sci.* 8, 251 (2004).
4. M. Calcagnotto, Y. Adachi, D. Ponge, and D. Raabe, *Acta Mater.* 59, 658 (2011).
5. R. Song, D. Ponge, D. Raabe, J.G. Speer, and D.K. Matlock, *Mater. Sci. Eng. A* 441, 1 (2006).
6. B.C. De Cooman, O. Kwon, and K.G. Chin, *J. Mater. Sci. Technol.* 28, 513 (2012).
7. M. Calcagnotto, D. Ponge, and D. Raabe, *ISIJ Int.* 48, 1096 (2008).
8. R. Song, D. Ponge, and D. Raabe, *Acta Mater.* 53, 4881 (2005).
9. Y. Sakuma, O. Matsumura, and O. Akisue, *ISIJ Int.* 31, 1348 (1991).
10. B.C. De Cooman and J.G. Speer, *Steel Res. Int.* 77, 634 (2006).
11. Y. Toji, H. Matsuda, M. Herbig, P.-P. Choi, and D. Raabe, *Acta Mater.* 65, 215 (2014).
12. F.G. Caballero, H.K.D.H. Bhadeshia, J.A. Mawella, D.G. Jones, and P. Brown, *Mater. Sci. Technol.* 17, 517 (2001).
13. D. Raabe, S. Sandlöbes, J. Millán, D. Ponge, H. Assadi, M. Herbig, and P.P. Choi, *Acta Mater.* 61, 6132 (2013).
14. D. Raabe, D. Ponge, O. Dmitrieva, and B. Sander, *Scripta Mater.* 60, 1141 (2009).
15. L. Yuan, D. Ponge, J. Wittig, P.P. Choi, J.A. Jiminez, and D. Raabe, *Acta Mater.* 60, 2790 (2012).
16. O. Grässel, L. Krüger, G. Frommeyer, and L.W. Meyer, *Int. J. Plast.* 16, 1391 (2000).
17. G. Frommeyer, U. Brüx, and P. Neumann, *ISIJ Int.* 43, 438 (2003).
18. G. Frommeyer and U. Brüx, *Steel Res. Int.* 77, 627 (2006).
19. O. Bouaziz, S. Allain, C.P. Scott, P. Cugy, and D. Barbier, *Curr. Opin. Solid State Mater. Sci.* 15, 141 (2011).
20. A. Saeed-Akbari, L. Mosecker, A. Schwedt, and W. Bleck, *Metall. Mater. Trans. A* 43, 1688 (2012).
21. J.E. Jin and Y.K. Lee, *Mater. Sci. Eng. A* 527, 157 (2009).
22. J.K. Kim, L. Chen, H.S. Kim, S.K. Kim, Y. Estrin, and B.C. Cooman, *Metall. Mater. Trans. A* 40, 3147 (2009).
23. S. Curtze and V.T. Kuokkala, *Acta Mater.* 58, 5129 (2010).
24. I. Gutierrez-Urrutia, S. Zaefferer, and D. Raabe, *Mater. Sci. Eng. A* 527, 3552 (2010).
25. H. Idrissi, K. Renard, D. Schryvers, and P.J. Jacques, *Scripta Mater.* 63, 961 (2010).
26. O. Bouaziz, S. Allain, and C. Scott, *Scripta Mater.* 58, 484 (2008).
27. H. Beladi, I.B. Timokhina, Y. Estrin, J. Kim, B.C. Cooman, and S.K. Kim, *Acta Mater.* 59, 7787 (2011).
28. H.K. Yang, Z.J. Zhang, and Z.F. Zhang, *Scripta Mater.* 68, 992 (2013).
29. D. Barbier, N. Gey, S. Allain, N. Bozzolo, and M. Humbert, *Mater. Sci. Eng. A* 500, 196 (2009).
30. I. Gutierrez-Urrutia, S. Zaefferer, and D. Raabe, *JOM* 65, 1229 (2013).
31. I. Gutierrez-Urrutia, S. Zaefferer, and D. Raabe, *Scripta Mater.* 61, 737 (2009).
32. I. Gutierrez-Urrutia and D. Raabe, *Scripta Mater.* 66, 992 (2012).
33. I. Gutierrez-Urrutia and D. Raabe, *Acta Mater.* 59, 6449 (2011).
34. I. Gutierrez-Urrutia and D. Raabe, *Scripta Mater.* 66, 343 (2012).
35. S. Reeh, D. Music, T. Gebhardt, M. Kasprzak, T. Jäpel, S. Zaefferer, D. Raabe, S. Richter, A. Schwedt, J. Mayer, B. Wietbrock, G. Hirt, and J.M. Schneider, *Acta Mater.* 60, 6025 (2012).
36. H. Kim, D.-W. Suh, and N.J. Kim, *Sci. Technol. Adv. Mater.* 14, 014205 (2013).
37. G. Frommeyer and U. Brüx, *Steel Res. Int.* 77, 627 (2006).
38. J.D. Yoo and K.-T. Park, *Mater. Sci. Eng. A* 496, 417 (2008).
39. K.M. Chang, C.G. Chao, and T.F. Liu, *Scripta Mater.* 63, 162 (2010).
40. K. Choi, C.-H. Seo, H. Lee, S.K. Kim, J.H. Kwak, K.G. Chin, K.-T. Park, and J. Kim, *Scripta Mater.* 63, 1028 (2010).

41. I. Gutierrez-Urrutia and D. Raabe, *Acta Mater.* 60, 5791 (2012).
42. S.Y. Han, S.Y. Shin, H.-J. Lee, B.-J. Lee, S. Lee, N.J. Kim, and J.-H. Kwak, *Metall. Mater. Trans. A* 43A, 843 (2012).
43. I. Gutierrez-Urrutia and D. Raabe, *Scripta Mater.* 68, 343 (2013).
44. Y. Kimura, K. Handa, H. Hayashi, and Y. Mishima, *Intermetallics* 12, 607 (2004).
45. J.-B. Seol, D. Raabe, P. Choi, H.-S. Park, J.-H. Kwak, and C.-G. Park, *Scripta Mater.* 68, 348 (2013).
46. C.Y. Chao, C.N. Hwang, and T.F. Liu, *Scripta Metall. Mater.* 28, 109 (1993).
47. C.N. Hwang, C.Y. Chao, and T.F. Liu, *Scripta Metall. Mater.* 28, 263 (1993).
48. I. Gutierrez-Urrutia and D. Raabe, *Mater. Sci. Technol.* 30, 1099 (2014).
49. H. Springer and D. Raabe, *Acta Mater.* 60, 4950 (2012).
50. D.R. Steinmetz, T. Japel, B. Wietbrock, P. Eisenlohr, I. Gutierrez-Urrutia, A. Saeed-Akbari, T. Hickel, F. Roters, and D. Raabe, *Acta Mater.* 61, 494 (2013).
51. F. Roters, D. Raabe, and G. Gottstein, *Acta Mater.* 48, 4181 (2000).
52. H. Mecking and U.F. Kocks, *Acta Metall.* 29, 1865 (1981).
53. U.F. Kocks, A.S. Argon, and M.F. Ashby, *Prog. Mater Sci.* 19, 1 (1975).
54. R.L. Fullman, *Trans. AIME.* 197, 447 (1953).
55. S. Mahajan and G.Y. Chin, *Acta Metall.* 21, 1353 (1973).
56. A. Saeed-Akbari, J. Imlau, U. Prahl, and W. Bleck, *Metall. Mater. Trans. A* 40A, 3076 (2009).
57. M. Koyama, E. Akiyama, T. Sawaguchi, D. Raabe, and K. Tsuzaki, *Scripta Mater.* 66, 459 (2012).
58. M. Koyama, E. Akiyama, K. Tsuzaki, and D. Raabe, *Acta Mater.* 61, 4607 (2013).
59. M. Koyama, H. Springer, S.V. Merzlikin, K. Tsuzaki, E. Akiyama, and D. Raabe, *Int. J. Hydrog. Energy* 39, 4634 (2014).